Heydari, E., Bagheri, P. and Zare-Behtash, H. (2022) Photonic-based time-resolved multipulse oxygen sensor. IEEE Sensors Journal, (doi: 10.1109/JSEN.2022.3177426).

There may be differences between this version and the published version. You are advised to consult the publisher's version if you wish to cite from it.

http://eprints.gla.ac.uk/271583/

Deposited on: 24 May 2022

Enlighten – Research publications by members of the University of Glasgow
http://eprints.gla.ac.uk

Photonic-based Time-resolved Multipulse Oxygen Sensor

E. Heydari *, P. Bagheri, and H. Zare-Behtash

***Abstract*— Oxygen is one of Earth's vital elements, and its accurate measurement is crucial in numerous scientific and medical applications. Photonic-based sensors have recently become the subject of great attention for oxygen measurements due to their highly promising characteristics. These include the lack of requirement for repetitive calibrations and replacement of parts, being contactless, their accuracy, and fast response, and the potential to fabricate such sensors in small sizes. Here, we develop a dissolved-oxygen sensor by integrating time-resolved photoluminescence spectroscopy employing an FPGA-controlled multi-pulse LED source and amplified fast photodetector mounted on a PCB, light-emitting platinum porphine complex embedded polystyrene molecular oxygen-sensing probe, and a two-site Stern-Volmer function for the sensing and calibration. The PCB excites the molecular probe with multiple 50 ns blue light pulses, and the emission lifetime is extracted using an exponential function based on the Levenberg-Marquardt nonlinear fitting. Complete characterization of the sensor, including its sensitivity, repeatability, stability, and response time, in addition to the temperature and altitude compensation, is implemented to achieve excellent dissolved-oxygen sensing functionality.**

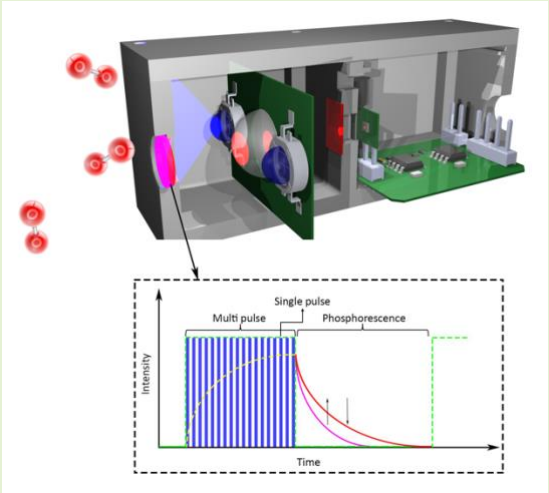

***Index Terms*— Multi-pulse LED, oxygen sensor, time-resolved phosphorescence spectroscopy, PtTFPP**

I. INTRODUCTION

Oxygen is considered one of the most important elements on Earth. For instance, the insufficient oxygen level in the human body, namely hypoxia, has a substantial effect on tissues and cells [1,2]. In cancerous tumors, the oxygen level is significantly lower than in normal tissues of the body [3]. Oxygen level is also essential in stem cell cultures [4]. Generally, controlling oxygen concentration is helpful in many cell culture applications due to the high impact of oxygen on the biological systems [5]. Other applications of oxygen sensors include measuring blood glucose levels, which is based on the oxidation of glucose oxidases [6-8]. The lack of oxygen in the human body causes problems in its normal functioning and, in severe cases, leads to diseases [9]. Several sensing technologies are developed to measure oxygen concentration, including electrochemical sensors based on amperometry, electroconductivity and potentiometry, chemical sensors based on Winkler titration, and photonic sensors based on photoluminescence (PL) spectroscopy. Since the Clark electrode was developed, it has become the most reliable and commonly used measurement technology [10]. However, the Clark electrode exhibits some disadvantages that have hindered its further applications, such as oxygen consumption during measurements, which is detrimental in low-concentration oxygen detection, the requirement for repetitive calibration, replacement of electrode and electrolyte, and the large size of the electrode significantly limiting its usage in many biomedical applications.

In recent years, photonic oxygen sensors have found new applications in the food industry for the quality control purposes [11], the pharmaceutical sector for drug discovery [12], in automotive and aviation for air conditioning [13], aquafarming for high-density production [14,15] and biomedical for imaging [16,17]. When oxygen-sensing probes (OSP) are optically excited, electrons absorb the incident photons' energy to transfer from the ground state to excited states. Subsequently, the electrons undergo intersystem crossing from a singlet state to a triplet state and relax by releasing phosphorescence emission. Since this involves rotation of electrons, which is less likely to occur, the phosphorescence lifetime is long [18]. When the surrounding oxygen molecules strike the excited OSP molecules, they quench the phosphorescence emission, which appears as quenching in the PL lifetime and intensity. The level of reduction depends on the corresponding oxygen concentration [19]. Since the oxygen molecules are initially in a triplet state, they receive the energy of the excited OSP molecules and become singlet oxygen molecules after any collision. The reactivity of singlet oxygen molecules is very

* E. Heydari is with the Faculty of Physics, Kharazmi University, Tehran, 15719-14911, Iran (e-mail: e.heydari@khu.ac.ir).

H. Zare-Behtash is with the James Watt School of Engineering, University of Glasgow, Glasgow, G12 8QQ, UK

P. Bagheri is a M.Sc. student in the Faculty of Physics, Kharazmi University, Tehran, 15719-14911, Iran

high in dense materials, and in a short time, they react with other oxygen molecules and turn into a triplet one [20]. Typically, metal complexes of Pt, Ru, and Pd are used to synthesize the OSPs. These probes exhibit phosphorescence emission with a long lifetime ranging from microseconds to a few milliseconds under an optical excitation [21]. Developing a sensor based on a nanosecond excitation laser source is expensive; therefore, we employ ultra-bright and inexpensive light-emitting diode (LED) light sources to tackle the cost, size, and performance barriers. The Stern-Volmer relation in equation (1) provides the oxygen concentration in photonics-based sensors in terms of PL lifetime and intensity ratio [22-29]:

$$\frac{I_0}{I} = \frac{\tau_0}{\tau} = 1 + K_{sv}[O_2] \quad (1)$$

where τ and I are the lifetime and intensity for a given oxygen concentration, τ_0 and I_0 are the lifetime and intensity at zero oxygen concentration, respectively. K_{sv} is the molecular quenching constant, and $[O_2]$ is the oxygen concentration. This equation represents a linear graph, however, in many systems, the OSP does not exhibit a linear behavior due to the heterogeneity of the metal complex in the oxygen probe. It is possible to use the Stern-Volmer multi-site model in these scenarios, described by equation 2 [30-32]:

$$\frac{I_0}{I} = \frac{\tau_0}{\tau} = \left[\sum_n \left(\frac{f_n}{1+K_{SVn}[O_2]}\right)\right]^{-1} \quad (2)$$

where f_n is the fraction of the metal complex available to oxygen, K_{SVn} is the quenching constant for each site, and n represents the number of available sites. The two-site model (n = 2) is often used to divide the probe into the outer surface with easier access, and the inner surface with more difficult access to the oxygen. The PL lifetime, despite the intensity, is an inherent property of the matter which does not depend on the metal complex concentration. In addition, it exhibits less sensitivity to the shape, the measurement setup, and instability of the excitation source, which is why this technique is preferred for accurate measurements [33]. The two modes of frequency-domain and time-domain are commonly used to measure the PL lifetime [34]. In the frequency domain, modulated light sources with variable intensity, such as a sinusoidal wave, are employed to excite the OSPs. Since the lifetime of the OSP changes, the corresponding phase and modulation change accordingly [35,36]. In the second method, the OSP is excited by short pulses of light in which its wavelength lies in the absorption band of the OSP. Then, time-resolved PL intensity is measured with a fast photodiode or charge-coupled device (CCD). The decay curve is fitted with an exponential function to calculate the PL lifetime. The Levenberg-Marquardt nonlinear fitting is an excellent algorithm to examine the PL lifetime accurately. This method minimizes the merit function to find the best parameters [37].

Controlling dissolved-oxygen (DO) concentration is one of the essential factors in aquafarms. If aquatic animals are kept in low oxygen conditions, they experience stress, limiting their growth, increasing susceptibility to disease, and even death. In addition, the solubility of oxygen is strongly influenced by the water temperature [38-45]. Here, we develop a time-resolved PL spectroscopy-based DO sensor for real-time, fast, and continuous monitoring of DO concentration using multi-pulse LED light sources and an amplified photodetector controlled by a field-programmable gate array (FPGA) microprocessor. Pt(II) meso-Tetra(pentafluorophenyl) porphine metal-organic complex embedded in a polystyrene matrix was used as a molecular sensing probe. After the design and fabrication of the sensor circuit board, critical parameters of sensitivity, repeatability, response-time, and stability considering temperature and altitude compensations demonstrate the excellent capability of the photonics-based DO sensor.

II. Materials and Methods

OSP preparation: Pt(II) meso-Tetra(pentafluorophenyl) porphine known as PtTFPP was purchased from Frontier and toluene, and polystyrene (PS) from Sigma Aldrich. 2 mg of a PtTFPP oxygen-sensitive substance was dissolved in 2 ml of toluene to prepare the OSP solution. Afterward, 0.1 g of PS was dissolved in 2 ml of toluene. Then, 100 µL of PS solution was mixed with 500 µL of PtTFPP. Finally, the mixture was poured onto a 1 cm × 1 cm glass substrate and placed in an oven at 80 °C for 12 h to prepare a film of OSP. Then, it was punched with a 9 mm biopsy punch.

Temperature-controlled chamber: The chamber was equipped with two peltier plates, heat sinks, fan, temperature sensor, water pump, N_2 and O_2 inlet, Arduino Uno, and oxygen sensor. This chamber has two peltiers, one to cool and the other to heat the water. The cooler peltier has a fan to cool down the hot side of the peltier to increase its efficiency. A water pump was used to circulate the water. The Arduino Uno board and LabVIEW software control the entire closed-loop system and can keep the chamber's temperature constant with a ± 0.15 °C accuracy.

Photoluminescence spectrum: PL spectrum of the probe was measured using a Thorlabs CCS100 optical spectrometer when it was excited by a blue LED light source.

Absorption spectrum: The absorption spectrum of the OSP was measured using Analytik Jena Specord 210 Plus spectrometer.

Board design: Altium Designer software was used for the printed circuit board (PCB) design. This design requires attention to the -3.3V switching power supply because this source can cause significant noise to the amplifiers and analog-to-digital converters. The PCB was fabricated by the "Alfa Madar Sanat" company. It is a double-layer copper board with a thickness of 35 µm. LTspice software by Analog Devices was used to perform the simulations.

III. Results and Discussion

PtTFPP was selected as the oxygen-sensitive metal-organic complex and PS as the oxygen-permeable matrix. PtTFPP shows excellent quantum yield and fast response to the oxygen variation. The OSP was prepared by dissolving PtTFPP and PS matrix in toluene solvent and casting it onto a glass slide to form a 1 mm thick film. Figure 1a shows the absorption (blue-green), and PL (red) spectra of the OSP and the excitation LED spectrum (dark blue). The absorption peaks are located at 392 nm and 405 nm, and the emission peak is at 652 nm. The surface profile of the OSP measured by the Natsyco NAMA AFM is shown as an inset. The LED emission peak at 403 nm lies in the absorption band of the OSP, which guarantees excellent optical excitation of the OSP molecules. Figure 1b shows the controller circuit board of the oxygen sensor. Figure 1b. 1 shows the nanosecond pulse generator providing a 3 A current for generating the 50 ns excitation light pulses. Figure 1b. 2 is the PtTFPP-based OSP excited with the multi-pulse LED source. Figure 1b. 3 shows the driver of the fast photodiode (PD), which receives the PL signal and amplifies it 20 times. Figure 1b. 4 is the universal serial bus (USB) to serial converter for transferring the data to a computer. Figure 1b. 5 shows the FPGA microprocessor controlling the function of each element on the board of the oxygen sensor. Figure 1b. 6 is the power source for driving the circuit board. Two 4 W high-power blue LEDs were used to generate a pulsed excitation source instead of the conventional nanosecond pulsed lasers. The LED light sources are much smaller, have a longer lifetime, and are cheaper than laser sources. The LEDs emit short pulses with an average full width at half maximum (FWHM) of 47 ns. The pulse parameters such as the pulse width, repetition rate, and the number of multi-pulses were controlled using the FPGA. In the designed circuit, there is a metal–oxide–semiconductor field-effect transistor (MOSFET) driver for increasing the voltage level and current of the FPGA pulses enabling the complete switching of the MOSFET. Two resistors and a capacitor were used in the input to produce a high current for driving the LEDs. The capacitor stores the electric charges and is instantly discharged when the switch is turned on to generate high current pulses. A fast inverted diode parallel to the LEDs passes the return current when the MOSFET is turned off to prevent any damage to the excitation LEDs. The idea behind the multi-pulse is to increase the LED radiation energy and consequently increase the PL emission of the OSP. Figure 1b. 3 shows the PD and two corresponding amplifiers. The output of the PD is a current with a typical output of 510 nA at the wavelength of 535 nm. A high-speed amplifier was used as a trans-impedance amplifier to convert and amplify the PD output current to a voltage. This PD was reverse biased to improve the response and linearity. A capacitor was placed parallel to the feedback resistor as a filter to limit the frequency response. In addition, a rail-to-rail amplifier was used to amplify the output further. A 12-bit converter capable of sampling up to 3 MS/s with an SPI serial connection was employed as an analog-to-

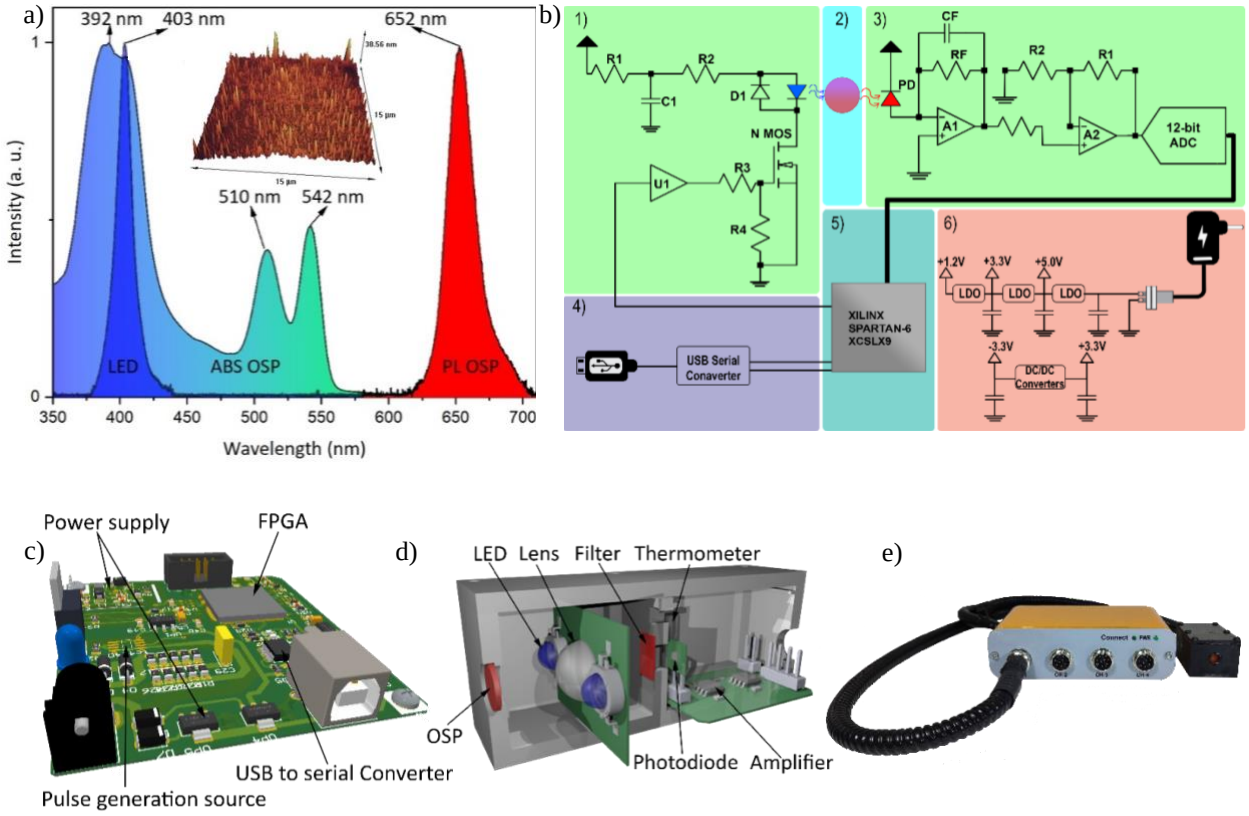

Fig. 1. a) Absorption (blue-green) and PL (red) spectra of the OSP. The dark blue color is the excitation LED spectrum. Inset is an AFM profile of the OSP. b) Schematic of photonic-based oxygen sensor circuit board: 1) Pulse generation source and MOSFET driver 2) The PtTFPP-based OSP film 3) The PD driver and amplifie rs 4) USB to serial converter 5) The FPGA microprocessor 6) Power supply c) Schematic of the PCB of the multipulse oxygen sensor d) Schematic of the optical detection section of the oxygen sensor consisting of the OSP, excitation LEDs, collecting and focusing lens, filter, thermometer, photodiode, and amplifier circuit e) final shape of the photonic-based oxygen sensor.

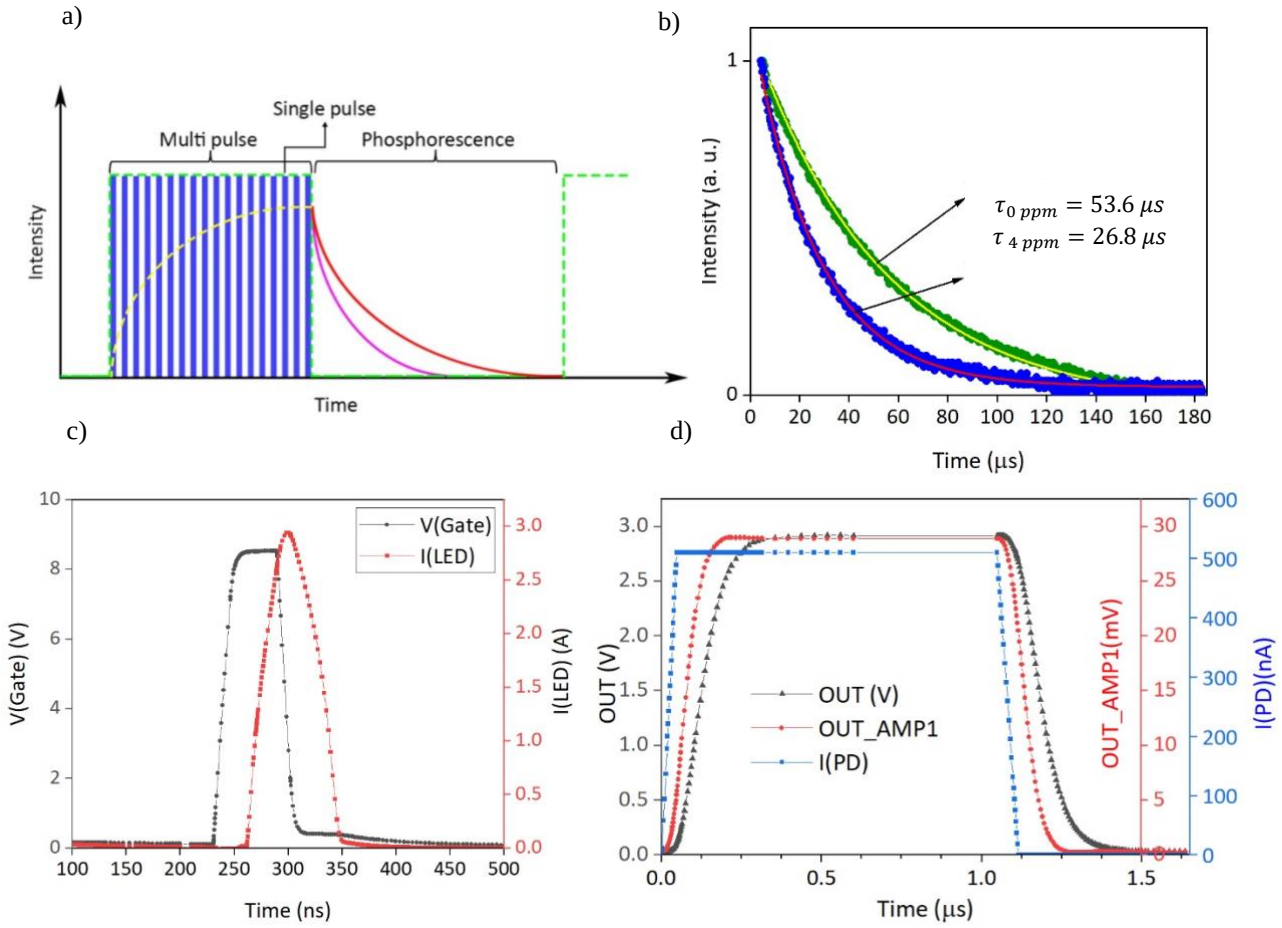

Fig. 2. a) Multi-pulse concept for the excitation of the OSP b) Lifetime measurement for two different concentrations c) Simulation of the output voltage of the MOSFET in black and the applied current to the LED in red d) Maximum current of the PD in the blue, output voltage of the first amplifier in red and output voltage of the second amplifier in black.

digital converter. An FPGA microprocessor from the Spartan-6 family was employed for processing the data. The processor was launched using an external 60 MHz external oscillator. A frequency higher than 60 MHz is required to run other components such as the analog to digital converter, USB to serial converter, and the pulse generator. Thus, the Intellectual Property Core Clocking Wizard by ISE Design Suite was used. This frequency was converted into two frequencies of 100 MHz and 46 MHz, where the 46 MHz was used for the analog-to-digital converter and the 100 MHz for the rest. The generated clocking network typically consists of a clocking primitive in addition to the buffers and clock pins. Distributed Memory was employed to receive PD information quickly and then transfer it to USB at a slower speed using a serial converter. The Distributed Memory Generator uses LUT-based distributed read-only memory (ROM) resources to create 16-bit deep, 1-bit wide ROMs and generates a fabric-based bus multiplexer to create a deeper and wider ROM. The content of this memory is defined by supplying an input coefficient (COE) file to the Vivado Design Suite. Because this system uses multiple clocks, first-in-first-out (FIFO) was used to eliminate cross clocking. FIFO is a memory that can store and organize information and then send the information with a deliberate clock. This microprocessor requires two voltages of 3.3 V and 1.2 V to operate, which were provided by a power supply shown in Figure 1b. 6. A direct current (DC)/DC converter supplies a negative voltage to drive the PD amplifiers. This converter operates at a frequency of 2.2 MHz which induces noise on the amplifiers. Therefore, keeping the power supply away from the amplifiers is necessary to eliminate this noise. For this reason, the power supply of the amplifiers was designed separately. A serial protocol could be used to transfer data from the microprocessor; however, nowadays, most computers are not equipped with a serial port. Therefore, a USB to CH 340 serial converter that can store data was used to convert the serial protocol to USB. Data are sent in packages to ensure the accuracy of the transferred information. The package consists of two fixed letters at the beginning, then data such as temperature, time, and PD information, and two other fixed letters at the end to indicate the completion of the package. Figure 1c illustrates different sections of the designed PCB. It consists of a microprocessor, nanosecond short pulse generator, and LED driver. Figure 1d depicts the optical section of the sensor consisting of the OSP, two excitation LEDs, collection lens, PD, and two amplifiers. Figure 1e shows the final image of the developed multi-pulse oxygen sensor.

Figure 2a presents a schematic of the multi-pulse excitation concept of the OSP, where the blue lines and green dash lines represent a single pulse and multi-pulse, respectively. The yellow line demonstrates the pumping of the triplet state, and

the red and purple lines represent the PL emission of the OSP for different oxygen concentrations. The lifetimes are achieved by fitting the PL decay curve by an exponential equation. A common approach for achieving a lifetime is the "pulse-and-gate" method. In this method, a part of the decay curve data is fitted instead of all the received data. Thus, it provides fast processing but higher errors [46,47]. Figure 2b depicts the PL decay curve of the OSP and the corresponding fitted curve for the oxygen concentrations of 0 ppm and 4 ppm. The PL lifetime is longer for lower oxygen concentrations due to less interaction with the oxygen molecules. The pulse generator circuit was simulated using the LTspice software where a pulse source, the so-called pulser, creates a pulse with a width of 50 ns, rise-time of 10 ns, and fall-time of 10 ns with a maximum voltage of 3 V. This pulse is then applied to a MOSFET driver to increase the pulse to 8.5 V, which is presented in Figure 2c in black. A high current is required to drive the LED in a short time. Figure 2c shows that the current passing through the LED in this time interval is approximately 3 A, which is indicated with a red line. In addition, simulations were performed for the amplifiers. Thus, a combination of a current source with a capacitor and resistor connected in parallel was used to simulate the PD, which produces a pulse with a maximum current of 510 nA. Then the first amplifier converts the current to voltage, and subsequently, the second amplifier increases it to 3 V. Figure 2d shows the simulation results where the blue line is the PD current. The red line represents the first amplifier's output voltage which is approximately 0.03 V. Next, the second amplifier increases this voltage to 3 V, shown with a black line. A graphical interface was written in LabVIEW for signal processing and displaying information such as the temperature and real-time DO concentration. In Figure 3a a typical sensor signal is demonstrated, comprising an excitation LED denoted by the blue color and a PL decay curve shown in red. The PL decay curve is fitted with an exponential function using the Levenberg-Marquardt algorithm, shown by the green curve.

SENSITIVITY

Next, the sensor was placed in a temperature and DO-controlled water chamber where two peltiers control the temperature with an accuracy of ± 0.15 ºC using a combination of an Arduino Uno and LabVIEW. The water chamber's temperature was maintained at 22.1 ºC, and the DO concentration was modified from 0 % to 200 % air saturation to calibrate it and obtain its Stern-Volmer diagram known as the sensor sensitivity or work function. First, N_2 gas was injected into the water chamber to reach 0 % air saturation, and then it was gradually increased during 2 h to reach 100 %. Afterward, O_2 gas was injected into the water chamber to reach 200 % saturation, and the rest was measured from 200 % to 100 % during the next 4 h. A Hanna Edge 2040 oxygen meter was employed for the calibration. Figure 3b demonstrates the Stern-Volmer diagram for the OSP,

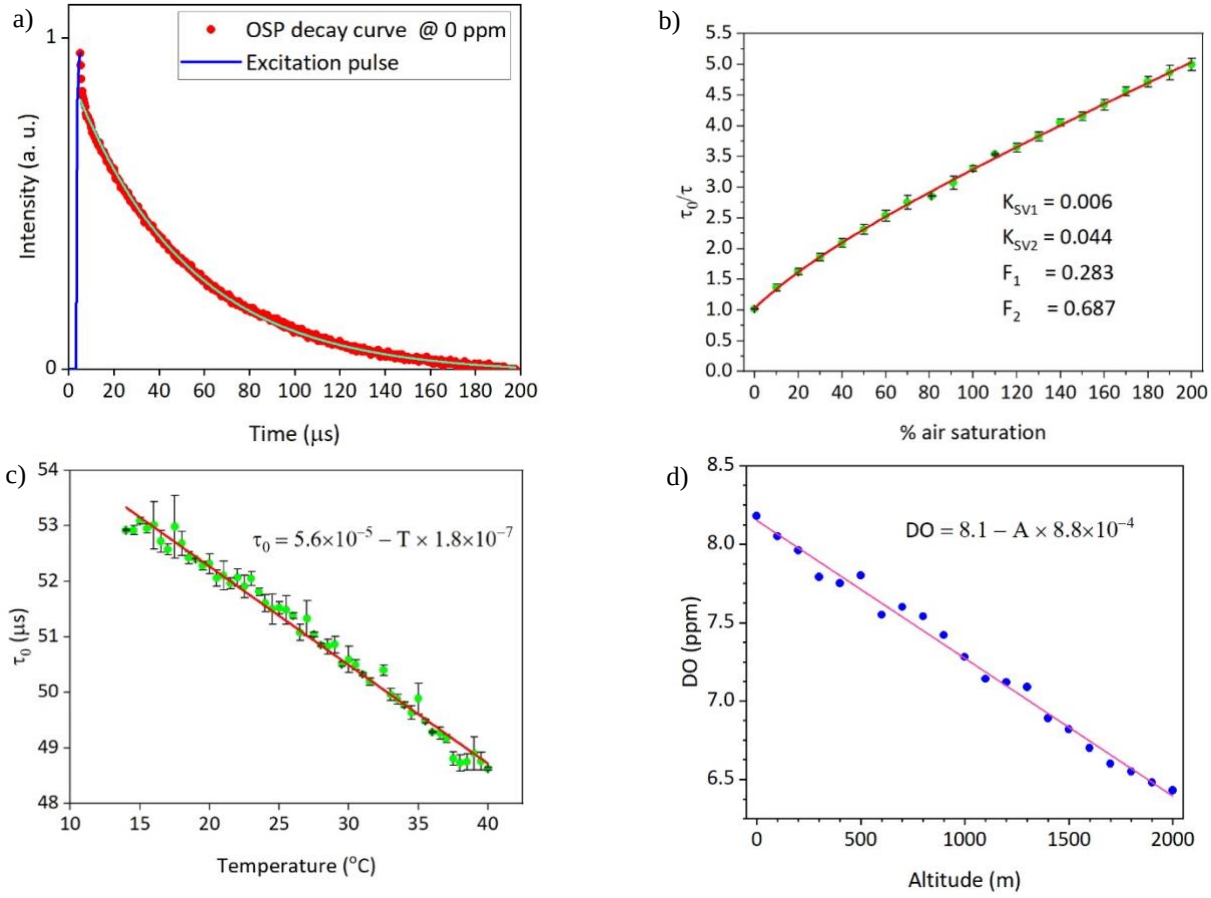

Fig. 3. a) Output signal of the OSP received by the PD. Blueline is the excitation pulse, and red is the PL decay curve. Pl decay curve is fitted with an exponential function to achieve the PL decay lifetime b) Stern-Volmer lifetime ratio based on the oxygen concentration d) Effect of temperature of the decay lifetime.

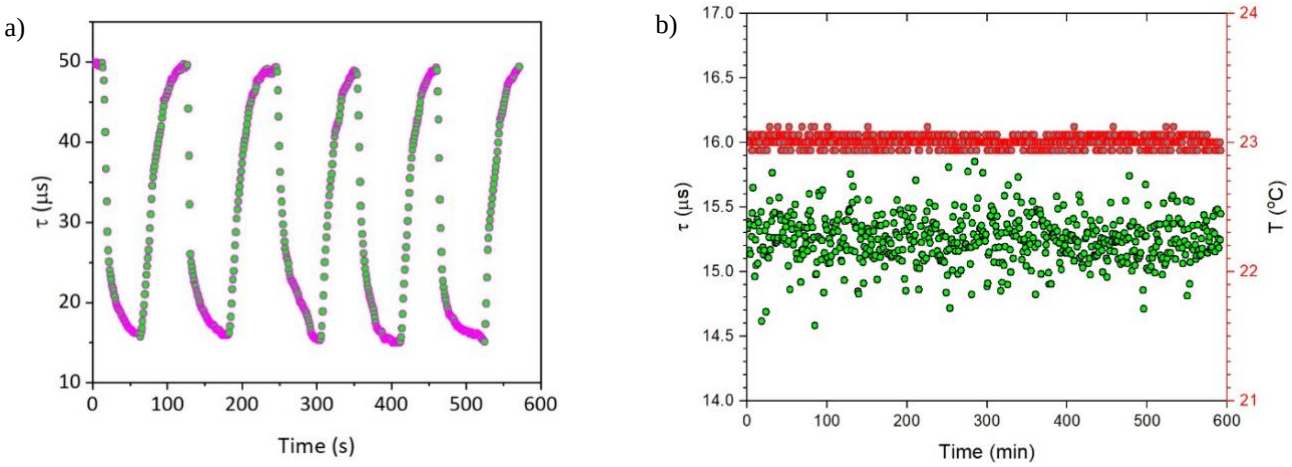

Fig. 4. a) Response time of the OSP for increasing air saturation percentage from 0 % to 100 % was 59 s and for 100 % to 0 % was 36 s b) Lifetime stability of the OSP (green circles) during 4 h measurement at 100 % air saturation and the corresponding temperature (red circles).

which is the lifetime ratio, $\frac{\tau_0}{\tau}$, based on the air saturation shown with green circles. This diagram deviated from a linear function. Thus, it was fitted with the two-site Stern-Volmer function indicated with a red curve based on the equation 2. Therefore, the Stern-Volmer parameters of $K_{SV1} = 0.006, K_{SV2} = 0.044, f_1 = 0.283\ and\ f_2 = 0.687$ and the sensor work function were achieved. For accurate measurements, it is necessary to find the compensation for the temperature and altitude affecting the DO concentration.

TEMPERATURE COMPENSATION

The OSP is susceptible to the ambient temperature affecting both τ_0 and K_{SV} [48]. In Figure 3c, the temperature-dependent PL lifetime in the range of 15 ºC to 40 ºC at the DO concentration of 0 ppm was investigated. It was observed that the lifetime linearly decreases with increasing temperature. The DO concentration was preserved in this experiment to avoid any possible interference. Equation 3 compensates for these two parameters [49,50]

$$O_2[ppm] = \frac{P_{atm}-P_w(T)}{P_N} \times \frac{\%\ air\ saturation}{100} \times 0.2095 \times \alpha(T) \times \frac{M_{O_2}}{V_{O_2}} \quad (3)$$

where P_{atm} is the atmospheric pressure, P_N is the standard pressure (1013 mbar), $P_w(T)$ is the water vapor pressure with saturated air at the temperature T, M_{O_2} is the molecular mass of oxygen ($32\ \frac{g}{mol}$), V_{O_2} molar volume of oxygen ($22.414\ \frac{L}{mol}$) and $\alpha(T)$ is the Bunsen coefficient which is a function of the temperature. The Bunsen coefficient expresses the solubility of oxygen at the temperature T and is defined by equation 4 [49].

$$\ln 10^3\ \alpha(T) = \frac{8.553\times10^3}{T} + 23.78 \ln T - 160.8 \quad (4)$$

In addition, the water vapor pressure as a function of the temperature is calculated by equation 5 [51],

$$P_w(T) = exp\left(52.57 - \frac{6690.9}{T} - 4.681 \times lnT\right) \quad (5)$$

and the air saturation is obtained using the introduced two-site Stern-Volmer function.

ALTITUDE COMPENSATION

Figure 3d shows the altitude-dependent DO when the altitude varies from 0 m to 2000 m above sea level. DO was reduced linearly, with increasing the altitude, from 8.2 ppm to 6.4 ppm. These temperature and altitude compensations enable the improvement of the accuracy of the OSP.

RESPONSE TIME

Another essential characteristic of the oxygen sensor is its response time. It is defined as the time it takes the sensor to reach 90 % of the maximum oxygen concentration. Therefore, two containers of water were prepared, one containing 0 % air saturation water and the other containing 100 % air saturation water. The sensor was placed in one of the containers, and after reaching the desired percentage, it was placed in the other container. Therefore, the response time for 0 % to 100 % air saturation is 59 s, and the response time for 100 % to 0 % air saturation is 36 s. The rise and fall times [52] based on Figure 4a are 22 s and 32 s, respectively.

REPEATABILITY

Repeatability is the ability of a sensor to perform a measurement multiple times. Repeatability depends on the accuracy of the measurement and the active components. Excellent repeatability for a sensor makes the measurement values closer to the actual value. Equation 6 is used to calculate the repeatability [53,54].

$$KSD = \frac{\sqrt{[\sum(x_i-\mu)^2]/N}}{\mu} \times 100 \quad (6)$$

where KSD is the repeatability, x_i is the measurement data, N is the number of measurements, and μ is the average value. Repeatability tests were performed by placing the OSP sensor in the water chamber with a constant temperature of 22 °C, where the air saturation was modulated several times by injection of the N_2 gas. These measurements were repeated between 0 % and 40 % air saturation, and the repeatability of

0.2 for 0 % air saturation and 0.5 for 40 % air saturation was achieved.

Stability

The stability of the OSP was performed by placing the OSP in the temperature-control chamber containing 100 % air saturation water at the temperature of 23 °C. Figure 4b demonstrates the stability data in green and temperature in red. The stability deviation was 3.9 % for 4 h measurement with 1 min time resolution. Finally, the interference by other gases on the function of the OSP has already been investigated which revealed negligible impact [55,56].

IV. Conclusion

We have introduced a multi-pulse dissolved-oxygen sensor by combining time-resolved photoluminescence spectroscopy based on an FPGA microprocessor-controlled LED light source and fast amplified photodetector, a PtTFPP metal-organic molecular oxygen-sensing probe, and two-site Stern-Volmer fitting function. After the design and assembly of the electronic and optical elements, the excellent performance of the sensor was demonstrated by evaluating its sensitivity, repeatability, response time, and stability, considering the temperature and altitude compensation.

Acknowledgment

The authors would like to thank the staff of Kharazmi University for their technical and administrative support.

References

[1] M. S. Goligorsky, “Making sense out of oxygen sensor,” *Circ. Res.*, vol. 86, no. 8, pp. 824–826, 2000, doi: 10.1161/01.RES.86.8.824.

[2] P. Bajpai, “Historical perspectives,” *Green Energy Technol.*, no. 1, pp. 15–20, 2021, doi: 10.1007/978-981-15-8779-5_2.

[3] M. Höckel and P. Vaupel, “Tumor hypoxia: Definitions and current clinical, biologic, and molecular aspects,” *J. Natl. Cancer Inst.*, vol. 93, no. 4, pp. 266–276, 2001, doi: 10.1093/jnci/93.4.266.

[4] M. Csete, “Oxygen in the Cultivation of Stem Cells,” *Ann. N. Y. Acad. Sci.*, vol. 1049, no. 1, pp. 1–8, May 2005, doi: 10.1196/annals.1334.001.

[5] S. M. Grist, L. Chrostowski, and K. C. Cheung, “Optical Oxygen Sensors for Applications in Microfluidic Cell Culture,” *Sensors*, vol. 10, no. 10, pp. 9286–9316, Oct. 2010, doi: 10.3390/s101009286.

[6] S. W. Gao, H. S. Peng, X. H. Wang, F. T. You, F. Teng, and H. X. Wang, “Preparation of photoluminescent enzymatic nanosensors for glucose sensing,” *Sensors Actuators, B Chem.*, vol. 222, pp. 638–644, 2016, doi: 10.1016/j.snb.2015.08.092.

[7] R. Chaudhari, A. Joshi, and R. Srivastava, “Oxygen sensing glucose biosensors based on alginate nano-micro systems,” *Nanosensors, Biosensors, Info-Tech Sensors Syst. 2014*, vol. 9060, p. 906005, 2014, doi: 10.1117/12.2044894.

[8] S. K. Vashist, “Non-invasive glucose monitoring technology in diabetes management: A review,” *Anal. Chim. Acta*, vol. 750, pp. 16–27, 2012, doi: 10.1016/j.aca.2012.03.043.

[9] G. L. Semenza, “Oxygen Sensing, Homeostasis, and Disease,” *N. Engl. J. Med.*, vol. 365, no. 6, pp. 537–547, Aug. 2011, doi: 10.1056/NEJMra1011165.

[10] M. Quaranta, S. M. Borisov, and I. Klimant, “Indicators for optical oxygen sensors,” *Bioanal. Rev.*, vol. 4, no. 2–4, pp. 115–157, 2012, doi: 10.1007/s12566-012-0032-y.

[11] S. Banerjee, C. Kelly, J. P. Kerry, and D. B. Papkovsky, “High throughput non-destructive assessment of quality and safety of packaged food products using phosphorescent oxygen sensors,” *Trends Food Sci. Technol.*, vol. 50, pp. 85–102, Apr. 2016, doi: 10.1016/j.tifs.2016.01.021.

[12] M. H. Rabinowitz, “Inhibition of Hypoxia-Inducible Factor Prolyl Hydroxylase Domain Oxygen Sensors: Tricking the Body into Mounting Orchestrated Survival and Repair Responses,” *J. Med. Chem.*, vol. 56, no. 23, pp. 9369–9402, Dec. 2013, doi: 10.1021/jm400386j.

[13] B. Pedras, G. Orellana, and M. N. Berberan-Santos, “Luminescence-Based Sensors for Aeronautical Applications,” 2019, pp. 389–411.

[14] Y. Wei, Y. Jiao, D. An, D. Li, W. Li, and Q. Wei, “Review of Dissolved Oxygen Detection Technology: From Laboratory Analysis to Online Intelligent Detection,” *Sensors*, vol. 19, no. 18, p. 3995, Sep. 2019, doi: 10.3390/s19183995.

[15] M. Li, R. Singh, M. S. Soares, C. Marques, B. Zhang, and S. Kumar, “Convex fiber-tapered seven core fiber-convex fiber (CTC) structure-based biosensor for creatinine detection in aquaculture” *Opt. Express*, vol. 30, no. 8, p. 13898-13914, 2022, doi: 10.1364/OE.457958.

[16] T. Yoshihara, Y. Hirakawa, M. Hosaka, M. Nangaku, S. Tobita, “Oxygen imaging of living cells and tissues using luminescent molecular probes” *Journal of Photochemistry and Photobiology C: Photochemistry Reviews*, vol. 30, p. 71-95, 2017, doi: 10.1016/j.jphotochemrev.2017.01.001.

[17] T. V. Esipova, M. J. P. Barrett, E. Erlebach, A. E. Masunov, B. Weber, S. A. Vinogradov, “Oxyphor 2P: A High-Performance Probe for Deep-Tissue Longitudinal Oxygen Imaging” *Cell Metabolism*, vol. 29, p. 736-744, 2018, doi: 10.1016/j.cmet.2018.12.022.

[18] Y. Amao, “Probes and Polymers for Optical Sensing of Oxygen,” *Microchim. Acta*, vol. 143, no. 1, pp. 1–12, Sep. 2003, doi: 10.1007/s00604-003-0037-x.

[19] D. B. Papkovsky and R. I. Dmitriev, “Biological detection by optical oxygen sensing,” *Chem. Soc. Rev.*, vol. 42, no. 22, pp. 8700–8732, 2013, doi: 10.1039/c3cs60131e.

[20] S. Mitra and T. H. Foster, “Photochemical oxygen consumption sensitized by a porphyrin phosphorescent probe in two model systems,” *Biophys. J.*, vol. 78, no. 5, pp. 2597–2605, 2000, doi: 10.1016/S0006-3495(00)76804-4.

[21] Y. V. Aulin, M. Van Sebille, M. Moes, and F. C. Grozema, “Photochemical upconversion in metal-based octaethyl porphyrin-diphenylanthracene systems,” *RSC Adv.*, vol. 5, no. 130, pp. 107896–107903, 2015, doi: 10.1039/c5ra20602b.

[22] H. Nishikiori, M. Takeshita, Y. Komatsu, H. Satozono, and K. Teshima, “Photon Upconverted Emission Based on Dye-Sensitized Triplet–Triplet Annihilation in Silica Sol–Gel System,” *ACS Omega*, vol. 3, no. 8, pp. 8529–8536, Aug. 2018, doi: 10.1021/acsomega.8b01107.

[23] P. Borowicz and B. Nickel, “Triplet-triplet annihilation in viscous solutions as an example of non-Fickian diffusion,” *J. Opt. Soc. Am. B*, vol. 22, no. 2, p. 315, Feb. 2005, doi: 10.1364/JOSAB.22.000315.

[24] X. Zou, T. Pan, L. Chen, Y. Tian, and W. Zhang, “Luminescence materials for pH and oxygen sensing in microbial cells–structures, optical properties, and biological applications,” *Crit. Rev. Biotechnol.*, vol. 37, no. 6, pp. 723–738, 2017, doi: 10.1080/07388551.2016.1223011.

[25] M. Sulkes and Z. Sulkes, “Measurement of luminescence decays: High performance at low cost,” *Am. J. Phys.*, vol. 79, no. 11, pp. 1104–1111, Nov. 2011, doi: 10.1119/1.3620415.

[26] R. J. S. M. Guerrero, A. Murray, and E. Charbon, “Photoluminescence Lifetime Sensor Pixels using SPADs and Silicon LEDs in Commercial CMOS,” in *2019 IEEE SENSORS*, Oct. 2019, vol. 2019-Octob, pp. 1–4, doi: 10.1109/SENSORS43011.2019.8956921.

[27] A. H. Shadfan, “Luminescence Lifetime Instrumentation Development for Multi-Dye Analysis,” 2011.

[28] G. Holst, O. Kohls, I. Klimant, B. König, M. Kühl, and T. Richter, “A modular luminescence lifetime imaging system for mapping oxygen distribution in biological samples,” *Sensors Actuators, B Chem.*, vol. 51, no. 1–3, pp. 163–170, 1998, doi: 10.1016/S0925-4005(98)00232-9.

[29] H. Boaz and G. K. Rollefson, “The Quenching of Fluorescence. Deviations from the Stern-Volmer Law,” *J. Am. Chem. Soc.*, vol. 72, no. 8, pp. 3435–3443, Aug. 1950, doi: 10.1021/ja01164a032.

[30] Y. Amao, T. Miyashita, and I. Okura, “Platinum tetrakis(pentafluorophenyl)porphyrin immobilized in polytrifluoroethylmethacrylate film as a photostable optical oxygen detection material,” *J. Fluor. Chem.*, vol. 107, no. 1, pp. 101–106, Jan. 2001, doi: 10.1016/S0022-1139(00)00352-3.

[31] Y. Mao, M. Akram, J. Shi, J. Wen, C. Yang, J. Jiang, Z. Lu, B. Zhou,

and Y. Tian, “Optical oxygen sensors based on microfibers formed from fluorinated copolymers,” *Sensors Actuators B Chem.*, vol. 282, pp. 885–895, Mar. 2019, doi: 10.1016/j.snb.2018.11.143.

[32] C. L. McNeil and E. A. D’Asaro, “A calibration equation for oxygen optodes based on physical properties of the sensing foil,” *Limnol. Oceanogr. Methods*, vol. 12, no. 3, pp. 139–154, Mar. 2014, doi: 10.4319/lom.2014.12.139.

[33] M. I. J. Stich, L. H. Fischer, and O. S. Wolfbeis, “Multiple fluorescent chemical sensing and imaging,” *Chem. Soc. Rev.*, vol. 39, no. 8, p. 3102, 2010, doi: 10.1039/b909635n.

[34] S. A. Pfeiffer and S. Nagl, “Microfluidic platforms employing integrated fluorescent or luminescent chemical sensors: A review of methods, scope and applications,” *Methods Appl. Fluoresc.*, vol. 3, no. 3, p. 34003, 2015, doi: 10.1088/2050-6120/3/3/034003.

[35] John Moore M.Sc., “Development of Enhanced Performance Luminescence-based Optical Sensor Systems for Single-analyte and Multi-analyte Applications,” Dublin City University, 2010.

[36] J. R. Lakowicz, *Principles of Fluorescence Spectroscopy*. Boston, MA: Springer US, 2006.

[37] G. Szentesi, G. Vereb, G. Horváth, A. Bodnár, A. Fábián, J. Matkó, R. Gáspár, S. Damjanovich, L. Mátyus, and A. Jenei, “Computer program for analyzing donor photobleaching FRET image series,” *Cytom. Part A*, vol. 67A, no. 2, pp. 119–128, Oct. 2005, doi: 10.1002/cyto.a.20175.

[38] C. E. Boyd and C. S. Tucker, *Pond Aquaculture Water Quality Management*. Boston, MA: Springer US, 1998.

[39] H. L. Atwood and D. C. Sandeman, *The Biology of Crustacea*. Elsevier, 1982.

[40] C. E. Boyd and C. S. Tucker, *Pond Aquaculture Water Quality Management*. Boston, MA: Springer US, 1998.

[41] P. Sriyasak, C. Chitmanat, N. Whangchai, J. Promya, and L. Lebel, “Effect of water de-stratification on dissolved oxygen and ammonia in tilapia ponds in Northern Thailand,” *Int. Aquat. Res.*, vol. 7, no. 4, pp. 287–299, Dec. 2015, doi: 10.1007/s40071-015-0113-y.

[42] C. Bett and L. Vinatea, “Combined effect of body weight, temperature and salinity on shrimp Litopenaeus vannamei oxygen consumption rate,” *Brazilian J. Oceanogr.*, vol. 57, no. 4, pp. 305–314, Dec. 2009, doi: 10.1590/S1679-87592009000400005.

[43] C. P. Madenjian, “Patterns of oxygen production and consumption in intensively managed marine shrimp ponds,” *Aquac. Res.*, vol. 21, no. 4, pp. 407–417, Dec. 1990, doi: 10.1111/j.1365-2109.1990.tb00479.x.

[44] A. Rajwa-Kuligiewicz, R. J. Bialik, and P. M. Rowiński, “Dissolved oxygen and water temperature dynamics in lowland rivers over various timescales,” *J. Hydrol. Hydromechanics*, vol. 63, no. 4, pp. 353–363, Dec. 2015, doi: 10.1515/johh-2015-0041.

[45] Chakravarty et al., “Spatial variation of water quality parameters of shrimp (Litopenaeus vannamei) culture ponds at Narsapurapupeta, Kajuluru and Kaikavolu villages of East Godavari district, Andhra Pradesh,” *Int. J. Fish. Aquat. Stud.*, vol. 4, no. 4, pp. 390–395, 2016.

[46] G. Liebsch, I. Klimant, B. Frank, G. Holst, and O. S. Wolfbeis, “Luminescence lifetime imaging of oxygen, pH, and carbon dioxide distribution using optical sensors,” *Appl. Spectrosc.*, vol. 54, no. 4, pp. 548–559, 2000, doi: 10.1366/0003702001949726.

[47] K. Kellner *et al.*, “Determination of oxygen gradients in engineered tissue using a fluorescent sensor,” *Biotechnol. Bioeng.*, vol. 80, no. 1, pp. 73–83, Oct. 2002, doi: 10.1002/bit.10352.

[48] N. Trivellin *et al.*, “Study and Development of a Fluorescence Based Sensor System for Monitoring Oxygen in Wine Production: The WOW Project,” *Sensors*, vol. 18, no. 4, p. 1130, Apr. 2018, doi: 10.3390/s18041130.

[49] T. Mock *et al.*, “Micro-optodes in sea ice: a new approach to investigate oxygen dynamics during sea ice formation,” *Aquat. Microb. Ecol.*, vol. 29, pp. 297–306, 2002, doi: 10.3354/ame029297.

[50] C. E. Boyd, E. L. Torrans, and C. S. Tucker, “Dissolved Oxygen and Aeration in Ictalurid Catfish Aquaculture,” *J. World Aquac. Soc.*, vol. 49, no. 1, pp. 7–70, Feb. 2018, doi: 10.1111/jwas.12469.

[51] T. L. Maurer, J. N. Plant, and K. N. Johnson, “Delayed-Mode Quality Control of Oxygen, Nitrate, and pH Data on SOCCOM Biogeochemical Profiling Floats” *Front. Mar. Sci.* vol. 8, pp. 1–20, 2021, 10.3389/fmars.2021.683207.

[52] R. Chen, C. E. W. Hahn, and A. D. Farmery, “A flowing liquid test system for assessing the linearity and time-response of rapid fibre optic oxygen partial pressure sensors,” *Respir. Physiol. Neurobiol.,* vol. 183, no. 2, pp. 100-107, Aug. 2012, doi: 10.1016/j.resp.2012.06.007.

[53] N. Bhalla, P. Jolly, N. Formisano, and P. Estrela, “Introduction to biosensors,” *Essays Biochem.*, vol. 60, no. 1, pp. 1–8, Jun. 2016, doi: 10.1042/EBC20150001.

[54] L.-C. Chen *et al.*, “Improving the reproducibility, accuracy, and stability of an electrochemical biosensor platform for point-of-care use,” *Biosens. Bioelectron.*, vol. 155, p. 112111, May 2020, doi: 10.1016/j.bios.2020.112111.

[55] C.-S. Chu and T.-H. Lin, “A new portable optical sensor for dual sensing of temperature and oxygen,” *Sensors Actuators B Chem., vol. 202, pp. 508–515, Oct. 2014, doi: 10.1016/j.snb.2014.05.125*.

[56] P. M. Gewehr and D. T. Delpy, “Optical oxygen sensor based on phosphorescence lifetime quenching and employing a polymer immobilised metalloporphyrin probe,” *Med. Biol. Eng. Comput., vol. 31, no. 1, pp. 2–10, Jan. 1993, doi: 10.1007/BF02446879.*

Esmaeil Heydari is an Assistant Professor in the Faculty of Physics, Kharazmi University, Tehran, Iran. He received his Ph.D. degree in Experimental Physics from the University of Potsdam in collaboration with the Fraunhofer Institute for Applied Polymer Research (IAP) in Germany, where he was an EU Marie-Curie Early-Stage Research fellow in the Dendreamers project. Afterward, he spent two years in the Biomedical Engineering Division at the University of Glasgow in Scotland as a Postdoctoral Research Assistant. Now he works with Kharazmi University, where he established the Nanophotonic Sensors and Optofluidics Laboratory to develop novel Nanobiophotonic Sensors.

Hossein Zare-Behtash was awarded a BEng (Hons) in Aerospace Engineering from UMIST. He continued from his final year individual project to do a Ph.D. in compressible Fluid Dynamics at the University of Manchester. He then took the role of Knowledge Transfer Fellow at the same university, working on short-term industry-led projects examining a broad range of experimental fluid dynamic phenomena, both compressible and incompressible. He joined Glasgow University as a Lecturer in 2013. Dr. Hossein Zare-Behtash is a Lecturer in the Aerospace Sciences Division of the James Watt School of engineering at UOG. He is one of the pioneering academics in the UK to develop and apply molecular sensing for the quantitative measurement of pressure and temperature in unsteady fluid dynamic phenomena, with a 15-year track record of investigating and using pressure and temperature-sensitive paints. His research expertise includes the development /application of advanced flow diagnostics, instrumentation, and specialized flow rigs.